

# Double and single pion photoproduction within a dynamical coupled-channels model

H. Kamano,<sup>1</sup> B. Juliá-Díaz,<sup>2,1</sup> T.-S. H. Lee,<sup>1,3</sup> A. Matsuyama,<sup>4,1</sup> and T. Sato<sup>5,1</sup>

<sup>1</sup>*Excited Baryon Analysis Center (EBAC),  
Thomas Jefferson National Accelerator Facility, Newport News, VA 23606, USA*

<sup>2</sup>*Department d'Estructura i Constituents de la  
Matèria and Institut de Ciències del Cosmos,  
Universitat de Barcelona, E-08028 Barcelona, Spain*

<sup>3</sup>*Physics Division, Argonne National Laboratory, Argonne, IL 60439, USA*

<sup>4</sup>*Department of Physics, Shizuoka University, Shizuoka 422-8529, Japan*

<sup>5</sup>*Department of Physics, Osaka University, Toyonaka, Osaka 560-0043, Japan*

## Abstract

Within a dynamical coupled-channels model which has already been fixed from analyzing the data of the  $\pi N \rightarrow \pi N$  and  $\gamma N \rightarrow \pi N$  reactions, we present the predicted double pion photoproduction cross sections up to the second resonance region,  $W < 1.7$  GeV. The roles played by the different mechanisms within our model in determining both the single and double pion photoproduction reactions are analyzed, focusing on the effects due to the direct  $\gamma N \rightarrow \pi\pi N$  mechanism, the interplay between the resonant and non-resonant amplitudes, and the coupled-channels effects. The model parameters which can be determined most effectively in the combined studies of both the single and double pion photoproduction data are identified for future developments.

PACS numbers: 13.75.Gx, 13.60.Le, 14.20.Gk

## I. INTRODUCTION

The spectrum and structure of low-lying nucleon and  $\Delta$  resonances (called collectively as  $N^*$ ) are primordial information for any understanding of the non-perturbative QCD domain. Consequently, a large effort has been made at the Excited Baryon Analysis Center (EBAC) during the past few years to extract the properties of  $N^*$  from the world data of  $\pi N \rightarrow \pi N$  and  $\gamma N \rightarrow \pi N$  data [1].

It is well acknowledged nowadays that a proper extraction and further interpretation of  $N^*$  properties requires the construction of reaction models which maintain the unitarity of most relevant channels, and can correlate the vast amount of data for both the single and double meson production reactions. Among the existing theoretical approaches, the one taken at EBAC tries to encompass the above by considering the interactions between the  $\gamma N$ ,  $\pi N$ ,  $\eta N$ , and  $\pi\pi N$  channels within a multi-channels multi-resonances framework [2]. After constraining the hadronic part of the model by fitting [3] the  $\pi N \rightarrow \pi N$  scattering data, we have performed our first studies of single pion photoproduction [4] and electroproduction reactions [5].

As discussed in our previous works, the hadronic part of the model was mostly constrained using  $\pi N \rightarrow \pi N$  experimental data. This means that the couplings of the  $N^*$  to the  $\pi\Delta$ ,  $\rho N$  and  $\sigma N$  channels, which are the quasi two-body channels of the  $\pi\pi N$ , are necessarily not well constrained in the current version of the model. To this extent, double pion photoproduction reactions are capital to understand the way  $N^*$  couple to the  $\pi\pi N$  channel, and thus to refine our global dynamical coupled-channels framework. In Ref. [6], we had carried out such a study for  $\pi N \rightarrow \pi\pi N$  reactions with the predicted cross sections in a reasonable agreement with the available data. In this work, we extend that work to investigate double pion photoproduction reactions by comparing our predictions with the total cross sections data [7, 8, 9, 10, 11, 12, 13] and invariant mass distributions [9, 10, 14]. We first present the predictions of our model for the double pion photoproduction reactions up to  $W=1.7$  GeV. We then analyze how the discrepancies with the data are sensitive to which of the electromagnetic parameters of the model, as a step toward performing the combined fits of the world data of  $\pi N, \gamma N \rightarrow \pi N, \pi\pi N$  reactions.

Most of the previous investigations of the double pion photoproduction reactions employed the tree diagram models [15, 16, 17, 18], emphasized the roles of certain resonances on specific double pion photoproduction reactions, or focussed on the very near threshold region using chiral perturbation theory [19, 20]. In our approach, we do not make such simplifications. We perform the full coupled-channels calculations and include all channels and  $N^*$  states determined in Refs. [3, 4].

The basic formulae used in this work are presented in Sec. II. In Sec. III we present the predictions of the current model and analyze the contributions from the direct  $\gamma N \rightarrow \pi\pi N$  mechanism and the transitions from  $\gamma N$  to the unstable  $\pi\Delta$ ,  $\sigma N$  and  $\rho N$  states. In Sec. IV we scrutinize the contribution of each of  $\gamma N \rightarrow N^*$  helicity amplitudes on both single pion and double pion photoproduction reactions. A summary and some conclusions are given in Sec. V.

## II. BASIC FORMULAE

Within the EBAC dynamical coupled-channels (EBAC-DCC) model, the  $\gamma N \rightarrow \pi\pi N$  amplitude consists of four pieces [2] (see Fig. 1):

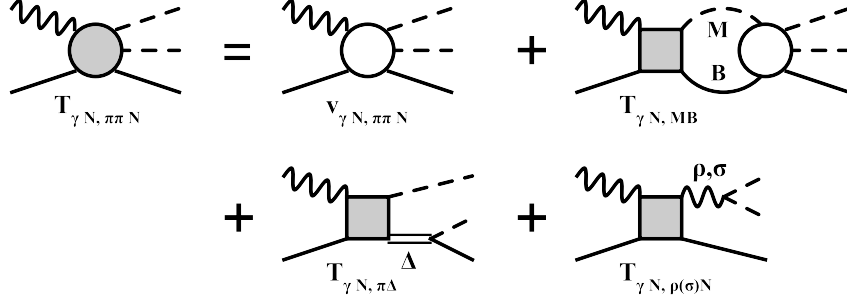


FIG. 1: Graphical representations of  $T_{\gamma N, \pi\pi N}$  of Eqs. (1)-(5).

$$T_{\gamma N, \pi\pi N}(E) = T_{\gamma N, \pi\pi N}^{\text{dir}}(E) + T_{\gamma N, \pi\pi N}^{\pi\Delta}(E) + T_{\gamma N, \pi\pi N}^{\rho N}(E) + T_{\gamma N, \pi\pi N}^{\sigma N}(E), \quad (1)$$

with

$$T_{\gamma N, \pi\pi N}^{\text{dir}}(E) = v_{\gamma N, \pi\pi N} + \sum_{MB} T_{\gamma N, MB}(E) G_{MB}(E) v_{MB, \pi\pi N}, \quad (2)$$

with,

$$T_{\gamma N, \pi\pi N}^{\pi\Delta}(E) = T_{\gamma N, \pi\Delta}(E) G_{\pi\Delta}(E) \Gamma_{\Delta \rightarrow \pi N}, \quad (3)$$

$$T_{\gamma N, \pi\pi N}^{\rho N}(E) = T_{\gamma N, \rho N}(E) G_{\rho N}(E) h_{\rho \rightarrow \pi\pi}, \quad (4)$$

$$T_{\gamma N, \pi\pi N}^{\sigma N}(E) = T_{\gamma N, \sigma N}(E) G_{\sigma N}(E) h_{\sigma \rightarrow \pi\pi}. \quad (5)$$

Here  $\Gamma_{\Delta \rightarrow \pi N}$ ,  $h_{\rho \rightarrow \pi\pi}$ , and  $h_{\sigma \rightarrow \pi\pi}$  describe the  $\Delta \rightarrow \pi N$ ,  $\rho \rightarrow \pi\pi$ , and  $\sigma \rightarrow \pi\pi$  decays, respectively;  $G_{MB}(E)$  ( $MB = \pi N, \eta N, \pi\Delta, \rho N, \sigma N$ ) are the meson-baryon Green's functions; The  $v_{\gamma N, \pi\pi N}$  are the direct  $\gamma N \rightarrow \pi\pi N$  transition potential illustrated in Fig. 2. The processes described by  $v_{\gamma N, \pi\pi N}$  are not contained in the  $T_{\gamma N, \pi\pi N}^{MB}$ , and thus there is no double counting.

The  $\gamma N \rightarrow MB$  transition amplitudes can be divided into the so-called non-resonant and resonant amplitudes (suppressing angular momentum, isospin, and momentum indices),

$$T_{\gamma N, MB}(E) = t_{\gamma N, MB}(E) + t_{\gamma N, MB}^R(E), \quad (6)$$

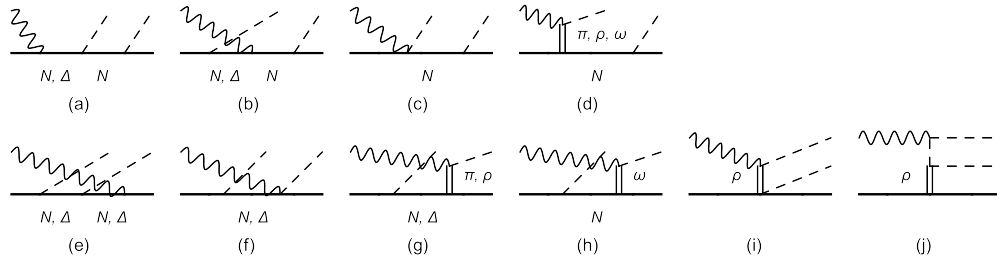


FIG. 2: Diagrams considered for  $v_{\gamma N, \pi\pi N}$ .

with

$$t_{\gamma N, MB}(E) = v_{\gamma N, MB} + \sum_{M'B'} v_{\gamma N, M'B'} G_{M'B'}(E) t_{M'B', MB}(E). \quad (7)$$

and

$$t_{\gamma N, MB}^R(E) = \sum_{N_i^*, N_j^*} \bar{\Gamma}_{\gamma N \rightarrow N_i^*}(E) [D(E)]_{i,j} \bar{\Gamma}_{N_j^* \rightarrow MB}(E). \quad (8)$$

In the above equation,  $v_{\gamma N, MB}$  represents the  $\gamma N \rightarrow MB$  transition potential which is derived from tree diagrams of a set of phenomenological Lagrangians describing the interactions among  $\gamma$ ,  $\pi$ ,  $\eta$ ,  $\rho$ ,  $\omega$ ,  $\sigma$ ,  $N$ , and  $\Delta(1232)$  fields. The details are given explicitly in Appendix F of Ref. [2]. The dressed  $\gamma N \rightarrow N^*$  vertex function appearing in Eq. (8) is defined by

$$\bar{\Gamma}_{\gamma N \rightarrow N^*}(E) = \Gamma_{\gamma N \rightarrow N^*} + \sum_{M'B'} v_{\gamma N, M'B'} G_{M'B'}(E) \bar{\Gamma}_{M'B' \rightarrow N^*}(E), \quad (9)$$

where  $\Gamma_{\gamma N \rightarrow N^*}$  denotes the bare  $\gamma N \rightarrow N^*$  vertex within the EBAC-DCC model, and is parametrized as

$$\Gamma_{N^*, \lambda_\gamma \lambda_N}^J(q) = \frac{1}{(2\pi)^{3/2}} \sqrt{\frac{m_N}{E_N(q)}} \frac{1}{\sqrt{2q}} [\sqrt{2q_R} A_\lambda^J] \delta_{\lambda, (\lambda_\gamma - \lambda_N)}, \quad (10)$$

where  $q_R$  is defined by the  $N^*$  mass  $M_{N^*} = q_R + E_N(q_R)$ .

Within our model, the meson-baryon Green function  $G_{MB}$ , the hadronic nonresonant amplitude  $t_{MB, M'B'}$ , the dressed  $N^*$  propagator  $D(E)$ , and the dressed  $N^* \rightarrow MB$  vertex function  $\bar{\Gamma}_{N^* \rightarrow MB}$  are purely hadronic processes. We take these hadronic pieces from the model constructed from analyzing the data of  $\pi N \rightarrow \pi N$  scattering [3], and keep them fixed throughout this paper.

The calculation of the terms  $T_{\gamma N \rightarrow \pi\pi N}^{MB}$  with  $MB = \pi\Delta, \rho N, \sigma N$ , defined by Eqs. (3)-(5), are straightforward. However, the calculation of the second term of  $T_{\gamma N \rightarrow \pi\pi N}^{\text{dir}}$ , defined by Eq. (2), is much more complex. To simplify the calculation, we employ the same prescription as in the calculation of the  $\pi N \rightarrow \pi\pi N$  reactions [6]. This is based on the observation that the processes (a)-(d) in Fig. 2 can be written as

$$v_{\gamma N, \pi\pi N}^{(\text{a-d})} \sim v_{\gamma N, \pi N} G_{\pi N}(E) h_{N \rightarrow \pi N}, \quad (11)$$

where  $v_{\gamma N, \pi\pi N}^{(\text{a-d})}$  is the sum of the all processes (a)-(d),  $v_{\gamma N, \pi N}$  is the 2-body  $\gamma N \rightarrow \pi N$  potential, and  $h_{N \rightarrow \pi N}$  is the  $N \rightarrow \pi N$  vertex function. Taking account of only a part of  $v_{MB, \pi\pi N}$  that can be approximately expressed as  $v_{MB, \pi\pi N} \sim v_{MB, \pi N} G_{\pi N}(E) h_{N \rightarrow \pi N}$ , Eq. (2) can be written as

$$\begin{aligned} T_{\gamma N, \pi\pi N}^{\text{dir}}(E) &\sim v_{\gamma N, \pi\pi N}^{(e-j)} + [v_{\gamma N, \pi N} + \sum_{MB} T_{\gamma N, MB}(E) G_{MB}(E) v_{MB, \pi N}] G_{\pi N}(E) h_{N \rightarrow \pi N} \\ &= v_{\gamma N, \pi\pi N}^{(e-j)} + T_{\gamma N, \pi N} G_{\pi N}(E) h_{N \rightarrow \pi N}. \end{aligned} \quad (12)$$

Here in the last step we have used the relation  $T_{\gamma N, \pi N} = v_{\gamma N, \pi N} + \sum_{MB} T_{\gamma N, MB} G_{MB} v_{MB, \pi N}$ . We use Eq. (12) which can be calculated with all parameters taken from our previous analysis of  $\pi N, \gamma N \rightarrow \pi N$  reactions.

The formulae for calculating total cross sections and invariant mass distributions from our amplitudes can be found in Ref. [6] and are not shown here.

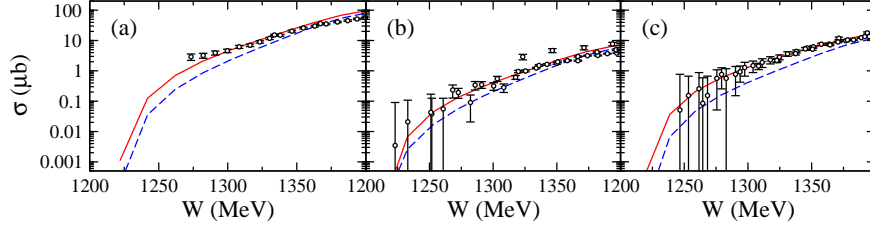


FIG. 3: Near threshold behavior of the total cross section for  $\gamma p \rightarrow \pi\pi N$ : (a)  $\gamma p \rightarrow \pi^+\pi^-p$ , (b)  $\gamma p \rightarrow \pi^0\pi^0p$ , and (c)  $\gamma p \rightarrow \pi^+\pi^0n$ . The red solid curve is the full results predicted from our current model, and the blue dashed curves are the results without the  $T_{\gamma N, \pi\pi N}^{\text{dir}}$  contribution. The data are taken from Refs. [7, 8, 9, 10, 11, 12, 13].

### III. ANALYSIS OF THE DIRECT REACTION MECHANISMS AND COUPLED-CHANNELS EFFECT

With the parameters determined from our previous analysis of  $\pi N, \gamma N \rightarrow \pi N$  reactions [3, 4], the results presented in this section are pure predictions within the current model developed in EBAC. We first present our results of the double pion photoproduction reactions, and then examine how the reactions mechanisms within our model determine the cross sections.

In Fig. 3, we find that our current model (red solid curve) has a good agreement with the  $\gamma N \rightarrow \pi\pi N$  total cross sections in the energy region up to  $W = 1.4$  GeV. We observe that the direct  $T_{\gamma N, \pi\pi N}^{\text{dir}}$  amplitude can greatly improve the model to reproduce the near threshold behavior of the  $\gamma N \rightarrow \pi\pi N$  total cross section data. Its effects in higher  $W$  are shown in the left panels [(a), (b), (c)] of Fig. 4. The red solid curves are the predictions from our full calculations and the blue dashed curves are from turning off the term  $T_{\gamma N, \pi\pi N}^{\text{dir}}$  (the bands in the figure will be explained later). We see that the effect of  $T_{\gamma N, \pi\pi N}^{\text{dir}}$  is sizable on  $\gamma p \rightarrow \pi^+\pi^-p$  [(a)] and  $\gamma p \rightarrow \pi^0\pi^0p$  [(b)], and negligible on  $\gamma p \rightarrow \pi^+\pi^0n$  [(c)]. It is clear that its inclusion does not change the energy dependence of the total cross sections for any of the considered  $\gamma N \rightarrow \pi\pi N$  reactions.

Although the threshold behavior is in general well reproduced as can be seen in Fig. 3, our predictions at higher  $W$  shown in Fig. 4 clearly overestimate the experimental data above  $W = 1.4$  GeV in both  $\gamma p \rightarrow \pi^+\pi^-p$ , and  $\gamma p \rightarrow \pi^0\pi^0p$  reactions, while the results of  $\gamma p \rightarrow \pi^+\pi^0n$  are good up to  $W = 1.5$  GeV. On the other hand, our current model reproduces the  $\gamma N \rightarrow \pi N$  reactions quite well in the considered energy region, as seen in the right panels of Fig. 4. This fact indicates that there exist reaction processes which have significant effect on the observables of  $\gamma N \rightarrow \pi\pi N$ , but not of  $\gamma N \rightarrow \pi N$ .

To get some insights into our disagreement with the data and to guide our future combined analysis of all  $\pi N, \gamma N \rightarrow \pi N, \pi\pi N$  reactions, we examine which mechanisms are most relevant to our calculations in this energy region. We first examine the contributions of each process appearing in Eqs. (2)-(5). The results from the full amplitude are shown in the top row of Fig. 5:  $T_{\gamma N, \pi\pi N}^{\pi\Delta}$  (black solid),  $T_{\gamma N, \pi\pi N}^{\sigma N}$  (red dashed),  $T_{\gamma N, \pi\pi N}^{\rho N}$  (green dotted), and  $T_{\gamma N, \pi\pi N}^{\text{dir}}$  (blue dash-dotted). The figures in the left, middle, and right columns are of the  $\gamma p \rightarrow \pi^+\pi^-p$ ,  $\gamma p \rightarrow \pi^0\pi^0p$ , and  $\gamma p \rightarrow \pi^+\pi^0n$  total cross sections, respectively.

We also show in the middle (bottom) row of Fig. 5 the results for which the full two-body amplitude  $T_{\gamma N, MB}$  in Eqs. (3)-(5) and (12) is replaced with its resonant (nonresonant)

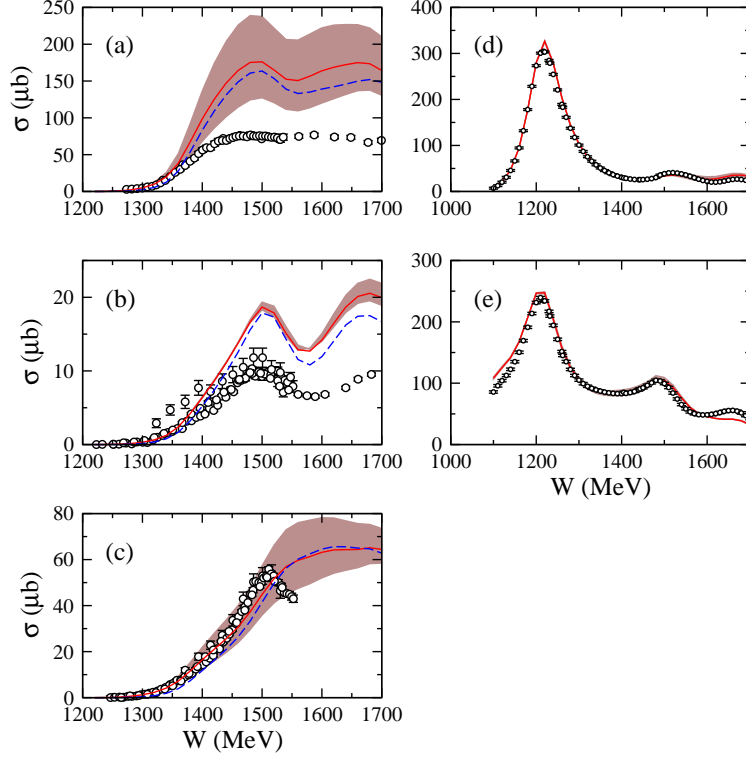


FIG. 4: Total cross sections of the double and single pion photoproduction reactions up to  $W = 1.7$  GeV: (a)  $\gamma p \rightarrow \pi^+ \pi^- p$ , (b)  $\gamma p \rightarrow \pi^0 \pi^0 p$ , (c)  $\gamma p \rightarrow \pi^+ \pi^0 n$ , (d)  $\gamma p \rightarrow \pi^0 p$ , and (e)  $\gamma p \rightarrow \pi^+ n$ . The red solid curve is the full result predicted from our current model, and the blue dashed curve in (a)-(c) is the result without  $T_{\gamma N, \pi \pi N}^{\text{dir}}$  contribution. The band is generated by allowing a 25% variation in the value of the  $\pi N \Delta$  coupling constant  $g_{\pi N \Delta}$  used in the electromagnetic amplitudes. The data of the double and single pion photoproduction reactions are taken from Refs. [7, 8, 9, 10, 11, 12, 13] and Refs. [21], respectively.

part  $T_{\gamma N, MB} \rightarrow t_{\gamma N, MB}^R$  ( $T_{\gamma N, MB} \rightarrow t_{\gamma N, MB}$ ). Thus we can examine the relative importance between different mechanisms in resonant  $t_{\gamma N, MB}^R$  and non-resonant  $t_{\gamma N, MB}$  amplitudes separately. Note that the curves describing  $\gamma N \rightarrow \sigma N$  ( $\gamma N \rightarrow \rho N$ ) process are not seen in the  $\gamma p \rightarrow \pi^+ \pi^0 n$  ( $\gamma p \rightarrow \pi^0 \pi^0 p$ ) total cross sections because the corresponding terms do not contribute due to isospin selection rules. In (a)-(c) of Fig. 5, we clearly see that the full  $\gamma N \rightarrow \pi \Delta \rightarrow \pi \pi N$  processes (black solid curves) have the largest contribution compared to the other processes. By comparing (a) and (g) of Fig. 5, we further find that the large discrepancy with the  $\gamma p \rightarrow \pi^+ \pi^- p$  data is mainly due to the nonresonant  $\gamma N \rightarrow \pi \Delta \rightarrow \pi \pi N$  amplitude. The dominance of the nonresonant  $\gamma N \rightarrow \pi \Delta \rightarrow \pi \pi N$  in all three  $\gamma N \rightarrow \pi \pi N$  reactions can also be seen in the bottom row panels of Fig. 5.

Most of the nonresonant  $\gamma N \rightarrow \pi \Delta$  transition matrix elements considered in our model depend on the  $\pi N \Delta$  coupling constant  $g_{\pi N \Delta}$  (see Ref. [2] for the details). We thus examine how our predictions are sensitive to this coupling strength. This is illustrated in Fig. 4 where we have presented bands, which are generated by varying  $g_{\pi N \Delta}$  included in the  $\gamma N \rightarrow \pi \Delta$  transition matrix elements by  $\pm 25\%$ . Clearly such changes in  $g_{\pi N \Delta}$  have a great influence on the  $\gamma p \rightarrow \pi^+ \pi^- p$  (top) and  $\gamma p \rightarrow \pi^+ \pi^0 n$  (bottom), and less for  $\gamma p \rightarrow \pi^0 \pi^0 p$  (middle). Within our dynamical coupled-channels model, the  $\gamma N \rightarrow \pi \Delta$  process also enters in the

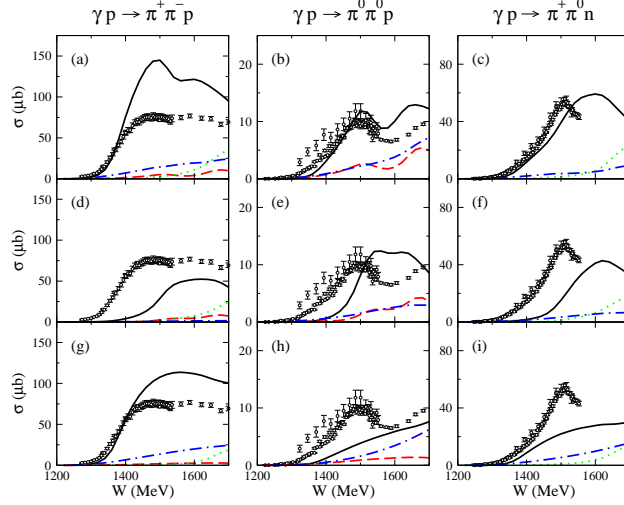


FIG. 5: Contributions of each reaction process described in Eqs. (2)-(5) to the total cross sections. (Black solid)  $\gamma N \rightarrow \pi\Delta$  contribution ( $T_{\gamma N, \pi\pi N}^{\pi\Delta}$ ); (red dashed)  $\gamma N \rightarrow \sigma N$  contribution ( $T_{\gamma N, \pi\pi N}^{\sigma N}$ ); (green dotted)  $\gamma N \rightarrow \rho N$  contribution ( $T_{\gamma N, \pi\pi N}^{\rho N}$ ); (blue dashed-dotted) the direct contribution ( $T_{\gamma N, \pi\pi N}^{\text{dir}}$ ). (Top row) Full results of each contribution; (Middle row) Results with the replacement of  $T_{\gamma N, MB} \rightarrow t_{\gamma N, MB}^R$ ; (Bottom row) Results with the replacement of  $T_{\gamma N, MB} \rightarrow t_{\gamma N, MB}$ . The data are taken from Ref. [7, 8, 9, 10, 11, 12, 13].

single pion photoproduction reactions as a consequence of the unitarity, and thus its change consistently affects the single pion photoproduction observables, too. As can be seen in the right panels of Fig 4, its importance turns out to be very minor in the  $\gamma N \rightarrow \pi N$  total cross sections. The bands from varying  $g_{\pi N \Delta}$  in  $\gamma N \rightarrow \pi\Delta$  by  $\pm 25\%$  are not visible. From this observation, in the following of this paper we will use a 20% smaller value for the  $g_{\pi N \Delta}$  appearing in the electromagnetic potentials. The value turns out to be very close to that of quark model.

In Figs. 6-8, we show the predicted invariant mass distributions of  $\gamma p \rightarrow \pi^+\pi^-p$ ,  $\gamma p \rightarrow \pi^0\pi^0p$ , and  $\gamma p \rightarrow \pi^+\pi^0n$ , respectively. To compare with the shapes of the data, the overall magnitudes of our predictions (red solid curves) are normalized to have the same integrated values of the data. We can see that the shapes of the predicted  $\pi N$  invariant mass distributions are in reasonable agreement with the data for all cases considered, while deviations are seen in several  $\pi\pi$  invariant mass distributions (right panels of Figs. 6-8).

This is found to be due to the fact that the  $\pi N$  distributions are dominated by the  $\Delta(1232)$  in the  $\gamma N \rightarrow \pi\Delta(1232) \rightarrow \pi\pi N$  process, while the  $\pi\pi$  distributions involve the interferences between all of the  $\gamma N \rightarrow \pi\Delta, \rho N, \sigma N \rightarrow \pi\pi N$  amplitudes. The results of the  $\pi\pi$  invariant mass distributions have provided useful information for improving our current model. In particular, the deviations from the data in the  $\pi^+\pi^0$  distributions of the  $\pi^+\pi^0n$  channel at high invariant mass (right panel of Fig.8) suggest that the parameters associated  $\rho N$  channels will need to be modified.

The most relevant novelty of the present study is the use of a dynamical coupled-channels model. In Fig. 9, we show the coupled-channels effects associated with the electromagnetic interactions on the  $\gamma N \rightarrow \pi\pi N$  total cross sections, which is demonstrated here for the first time in the investigations of double pion photoproduction reactions. The red solid curves are our full results. The green dotted curves are the results in which only the diagonal part

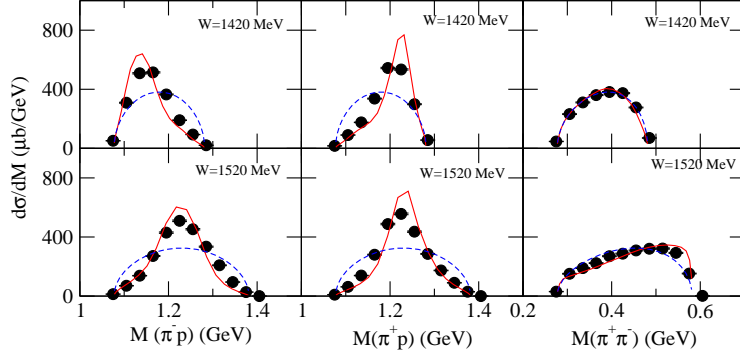


FIG. 6: Invariant mass distributions of  $\gamma p \rightarrow \pi^+ \pi^- p$  at  $W = 1420, 1520$  MeV: (left)  $(\pi^- p)$ ; (middle)  $(\pi^+ p)$ ; (right)  $(\pi^+ \pi^-)$ . The red solid curve is the full result, and the blue dashed curve is the phase space distribution. The magnitude of both curves is normalized to the data. The data are taken from Ref. [14].

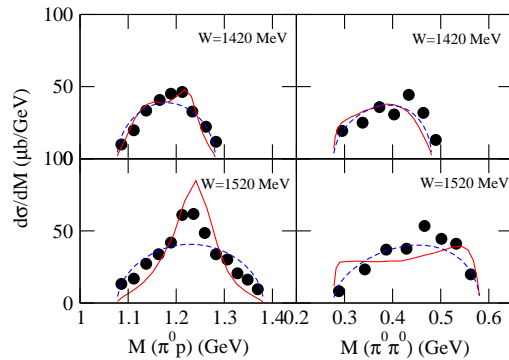


FIG. 7: Invariant mass distributions of  $\gamma p \rightarrow \pi^0 \pi^0 p$  at  $W = 1420, 1520$  MeV: (left)  $(\pi^0 p)$ ; (right)  $(\pi^0 \pi^0)$ . The red solid curve is the full result, and the blue dashed curve is the phase space distribution. The magnitude of both curves is normalized to the data. The data are taken from Ref. [9]. The energy bins of the data are 20-30 MeV around the central  $W$  shown in the panels.

( $M'B' = MB$ ) is taken in the  $M'B'$  summation of Eqs. (7) and (9), and the blue dashed curves are obtained by further setting  $t_{\gamma N, MB} \rightarrow v_{\gamma N, MB}$  and  $\bar{\Gamma}_{\gamma N \rightarrow N^*} \rightarrow \Gamma_{\gamma N \rightarrow N^*}$ . These correspond to examining the coupled-channels effect associated with the electromagnetic interactions. (Note again that the pure hadronic part of the amplitudes is fixed with the model determined in Ref. [3] throughout this paper.) In the considered energy region up to  $W = 1.7$  GeV, we find that the green dotted curves are far from the original results compared to the blue dashed curves. This shows not only the importance of the coupled-channels mechanisms, but also its very complex nature in the double pion photoproduction reactions.

#### IV. EFFECTS OF RESONANCES

The bare helicity amplitudes, defined in Eq. (10), are free parameters in our framework. They quantify the photoexcitation of the core  $N^*$  states and, together with their dressed counterparts, are to be interpreted by means of microscopic models, e.g. quark models,



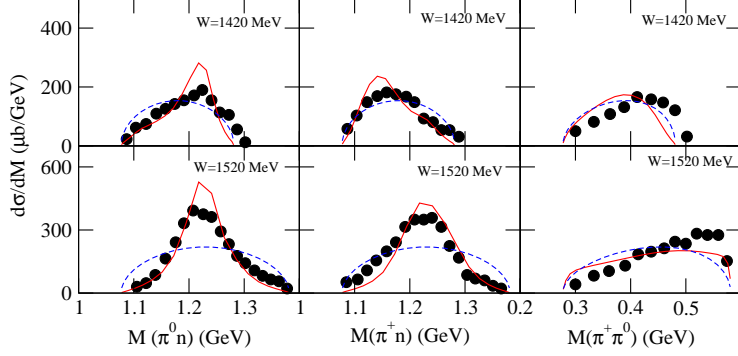


FIG. 8: Invariant mass distributions of  $\gamma p \rightarrow \pi^+ \pi^0 n$  at  $W = 1420, 1520$  MeV: (left)  $(\pi^0 n)$ ; (middle)  $(\pi^+ n)$ ; (right)  $(\pi^+ \pi^0)$ . The red solid curve is the full result, and the blue dashed curve is the phase space distributions. The magnitude of both curves is normalized to the data. The data are taken from Ref. [10]. The energy bins of the data are 20-30 MeV around the central  $W$  shown in the panels.

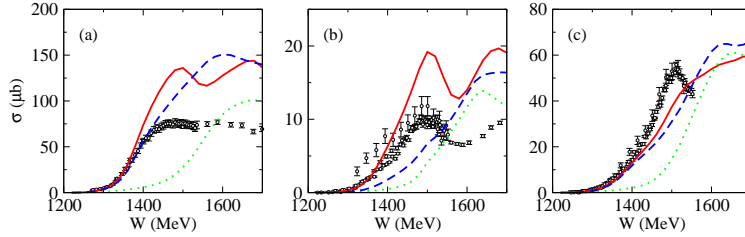


FIG. 9: Coupled-channels effects associated with electromagnetic interactions. The red solid curve is full results, the green dotted curve corresponds to taking only the diagonal element in the  $M'B'$  summation in Eqs. (7) and (9), and the blue dashed curve is obtained by further making a replacement of  $t_{\gamma N, MB} \rightarrow v_{\gamma N, MB}$  and  $\bar{\Gamma}_{\gamma N \rightarrow N^*} \rightarrow \Gamma_{\gamma N \rightarrow N^*}$ . The data are taken from Ref. [7, 8, 9, 10, 11, 12, 13].

lattice QCD calculations. Although  $A_\lambda^J$  are taken to be real numbers, the dressed helicity amplitudes, which have in general a sizeable contribution from the second term in Eq. (9), are complex numbers. This second term contains the meson-cloud contribution to the  $\gamma N N^*$  vertex, which is to a large extent fixed from the strong interaction sector.

In this section we present the effect on the single and double pion photoproduction observables of variations on the bare helicity amplitudes, which affect directly the dressed ones, see Eq. (9). This will be done by presenting results computed by varying the initial value of the bare helicity amplitudes listed in Table I, by  $\pm 50\%$ . The results are presented as bands in the figures, these bands are generated by filling the region enclosed by curves from two calculations using  $0.5 \times A_{j/2}$  and  $1.5 \times A_{j/2}$ .

Before proceeding to showing our results, we comment on the bare helicity amplitudes presented in Table I. Those values are not exactly the same as those of our previous  $\gamma N \rightarrow \pi N$  analysis [4]. They have been obtained by refitting the photoproduction data after corrections on the codes and are in most cases compatible with the previous values.

### A. S-wave $N^*$ s

We start the comparison with the  $S_{11}(1535)$  and  $S_{31}(1620)$ . In Fig. 10 we show the effect of varying their helicity amplitudes on the single pion photoproduction data. The sample data we consider are the total cross sections (left panel) for  $\gamma p \rightarrow \pi^0 p$  and  $\gamma p \rightarrow \pi^+ n$ , differential cross sections and polarization data in the  $\Delta(1232)$  region (central panel) and in the  $W=1500$  MeV region (right panel).

First we note that the  $\pm 50\%$  change in helicity amplitudes for the  $S_{11}(1535)$  resonance plays an important role in building the peak near 1500 MeV region for both  $\gamma p \rightarrow \pi^+ n, \pi^0 p$  total cross sections, see panels (a) and (f) of Fig. 10, and correspondingly in the differential cross section near the 1500 MeV region, see panels (c) and (h). The  $S_{31}$  gives a prominent contribution in the whole energy region above the  $\Delta(1232)$  region, as indicated by the oblique-lined bands. The  $S_{31}$  also affects the forward peaking of the  $\gamma p \rightarrow \pi^+ n$  differential cross section data around  $W=1500$  MeV, see panel (h). Their influence on the  $P$  observable is sizeable and qualitatively similar for both resonances, being negligible in the  $\Delta(1232)$  region.

Now we turn to the double pion photoproduction reactions, see left column of Fig. 11. First, as expected, and the same occurs for all resonances considered, the helicities have no influence on the near threshold behavior. Second, both S-wave resonances play a relevant role for the considered reactions. Modifying the  $A_{1/2}$  of the  $S_{11}(1535)$ , the total cross sections for the  $\gamma p \rightarrow \pi^0 \pi^0 p$  and  $\gamma p \rightarrow \pi^+ \pi^0 n$  can vary up to 20%, although there is no qualitative change in the energy dependence of the total cross sections, see panels (b) and (c) of Fig. 11. The  $S_{31}$  case is similar, but actually affects all the reactions. A smaller value of the  $S_{31}$  helicity amplitude is suggested by these results. Within our model, none of the peaks seen in the total cross section data can be ascribed solely to S-wave resonances.

TABLE I: The bare  $\gamma N \rightarrow N^*$  helicity amplitudes determined from  $\chi^2$ -fits to the  $\gamma N \rightarrow \pi N$ . The asterisk in the second (third) column marks the  $N^*$  states of which  $\gamma N$  transition process is found to be relevant to the single (double) pion photoproduction reactions up to  $W = 1.7$  GeV.

Bare $N^*$	$\gamma N \rightarrow \pi N$	$\gamma N \rightarrow \pi \pi N$	$A_{1/2}[10^{-3} \text{ GeV}^{-1/2}]$	$A_{3/2}[10^{-3} \text{ GeV}^{-1/2}]$
$S_{11}(1535)$	*	*	100	—
$S_{11}(1650)$			-19	—
$S_{31}(1620)$	*	*	203	—
$P_{11}(1440)$			-17	—
$P_{13}(1720)$			-53	-21
$P_{33}(1232)$	*		-78	-129
$D_{13}(1520)$	*	*	44	-60
$D_{15}(1675)$			54	30
$D_{33}(1700)$			0.3	-64
$F_{15}(1680)$	*		-82	-69

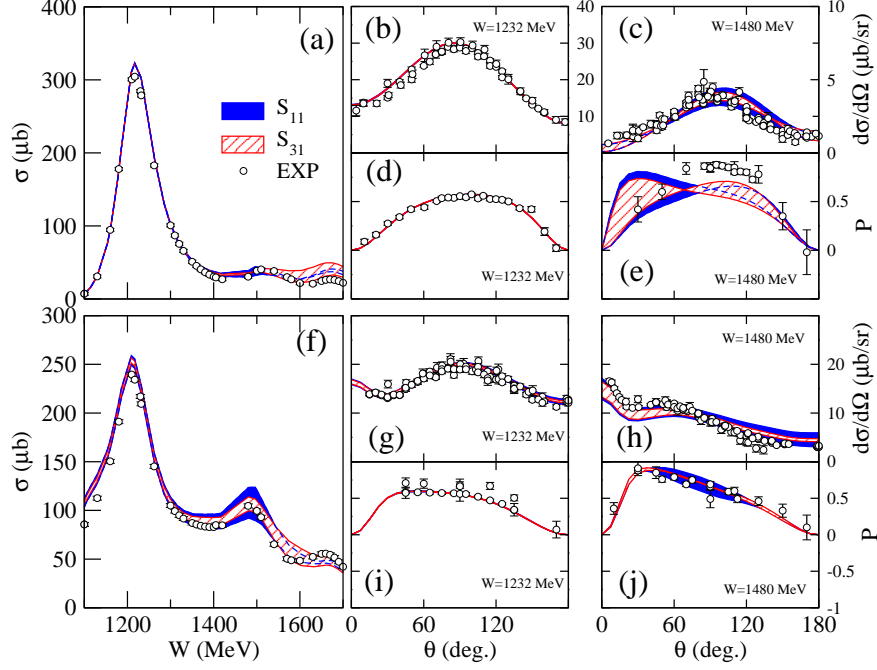


FIG. 10: The panels (a)-(e) depict the total cross section, differential cross sections and  $P$  polarization for  $\gamma p \rightarrow \pi^0 p$ , and (f)-(j) show total cross section, differential cross sections and  $P$  polarization for  $\gamma p \rightarrow \pi^+ n$ . Each band is obtained by allowing a 50% variation of the helicity amplitudes for the  $A_{1/2}$  of  $S_{11}(1535)$  (solid blue) and  $A_{1/2}$  of  $S_{31}(1620)$  (oblique-lined red) listed in Table I. The data are taken from Ref. [21].

### B. P-wave $N^*$ s

The helicity amplitudes of the  $\Delta(1232)$  resonance are essentially fixed by analyzing data near its nominal mass, as has long been known. In Fig. 12 we fully confirm this. The effect of variations on both  $A_{1/2}$  and  $A_{3/2}$  of the  $\Delta(1232)$  is well localized around its peak but reaches up to 300 MeV above it in the  $\gamma p \rightarrow \pi^0 p$  reaction, see panels (a)-(e). This can also be seen in their influence on the  $P$  asymmetry at  $W=1480$  MeV. The  $A_{3/2}$  mostly affects the perpendicular angles, while the  $A_{1/2}$  affects the forward and backward angles. The Roper resonance plays a minor role, with no sizeable trace in the observables.

In the double pion photoproduction case however, see middle column of Fig. 11, the  $\gamma N$  transition processes both of  $P_{33}$  and  $P_{11}$  play almost no role in the entire considered region. Let us point out that we refer here to the influence of the  $P_{33}$  as an s-channel exchange, the importance of the  $\Delta$  in this reaction is of course large, as pointed out in Sec. III where we have showed that most of the reaction flows through the  $\pi\Delta$  channel.

### C. D and F-wave $N^*$ s

Let us first study the influence of the helicity amplitudes on the single pion photoproduction. The  $D_{13}$  is responsible for part of the second peak near 1500 MeV in the  $\gamma p \rightarrow \pi^+ n$  total cross sections, see (f) of Fig. 13. The  $F_{15}(1680)$  contributes to the third peak in both total cross sections. In the central and right panels of Fig. 13, we see that none of the  $\pm 50\%$

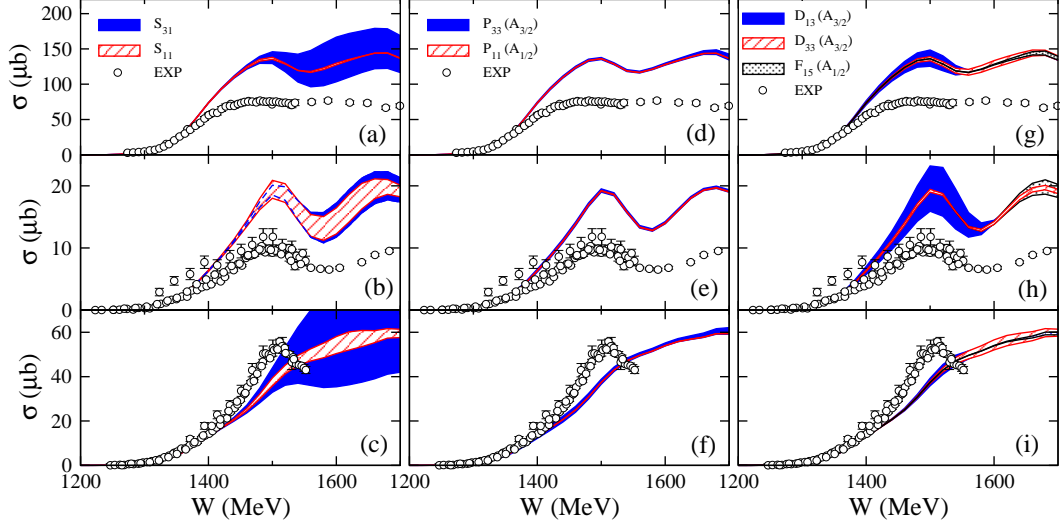


FIG. 11: Total cross sections, (a, d, g)  $\gamma p \rightarrow \pi^+ \pi^- p$ , (b, e, h)  $\gamma p \rightarrow \pi^0 \pi^0 p$ , and (c, f, i)  $\gamma p \rightarrow \pi^+ \pi^0 n$ . The different bands are generated by allowing  $\pm 50\%$  variations of the helicity amplitudes listed in Table I. The data are taken from Ref. [7, 8, 9, 10, 11, 12, 13].

changes of  $D_{13}$ ,  $F_{15}$  and  $D_{33}$  helicity amplitudes affect much the  $P$  and  $d\sigma/d\Omega$  observables.

$D$  wave resonances have long been advocated as being responsible for most of the structure observed in the total cross sections for  $\gamma p \rightarrow \pi\pi N$ . The first peak in the total cross sections has been explained in tree level calculations thanks to the  $D_{13}(1520)$  [15, 16, 18] and to interferences with the  $D_{33}(1700)$  [17]. In our coupled-channels model we confirm the very important role played by the  $D_{13}(1520)$  which builds up a large fraction of the first peak in the  $\gamma p \rightarrow \pi^0 \pi^0 p$  reaction, see the right part of Fig. 11. On the other hand its effect is also sizeable on the  $\gamma p \rightarrow \pi^+ \pi^- p$  total cross section, producing an overprediction of this observable in our model. As in the tree diagram models of Ref. [15, 16, 18] the peak structure in this reaction is always much more pronounced in the models than in the experimental data. Effects of the  $D_{33}$  are only sizeable on the  $\gamma p \rightarrow \pi^+ \pi^0 n$ , similarly to what was reported in Ref. [17], but they do not produce a peak structure as the experimental data show.

## V. SUMMARY AND CONCLUSIONS

Within the dynamical coupled-channels model constructed from analyzing the single pion production reactions [3, 4], we have investigated the total cross sections and the invariant mass distributions for the double pion photoproduction reactions off the proton in the energy region up to  $W = 1.7$  GeV. In the low energy region up to  $W = 1.4$  GeV, our results agree well with the total cross sections data, in which the direct process  $T_{\gamma N, \pi\pi N}^{\text{dir}}$  plays a crucial role for the reproduction of the data. Above  $W = 1.4$  GeV, our current model starts to overestimate the data for  $\gamma p \rightarrow \pi^+ \pi^- p$  and  $\gamma p \rightarrow \pi^0 \pi^0 p$ . We have found that the  $\gamma N \rightarrow \pi\Delta$  process is most relevant for the  $\gamma N \rightarrow \pi\pi N$  reactions and is a major origin of the overestimation in the  $\gamma p \rightarrow \pi^+ \pi^- p$  total cross section. Our model reproduces well the shapes of the invariant mass distributions data except several  $\pi\pi$  invariant mass distributions of  $\gamma p \rightarrow \pi^0 \pi^0 p$  and  $\gamma p \rightarrow \pi^+ \pi^0 n$ . We expect that this deviation provides useful information to improve our current model. Also, we have demonstrated the coupled-channels effects on

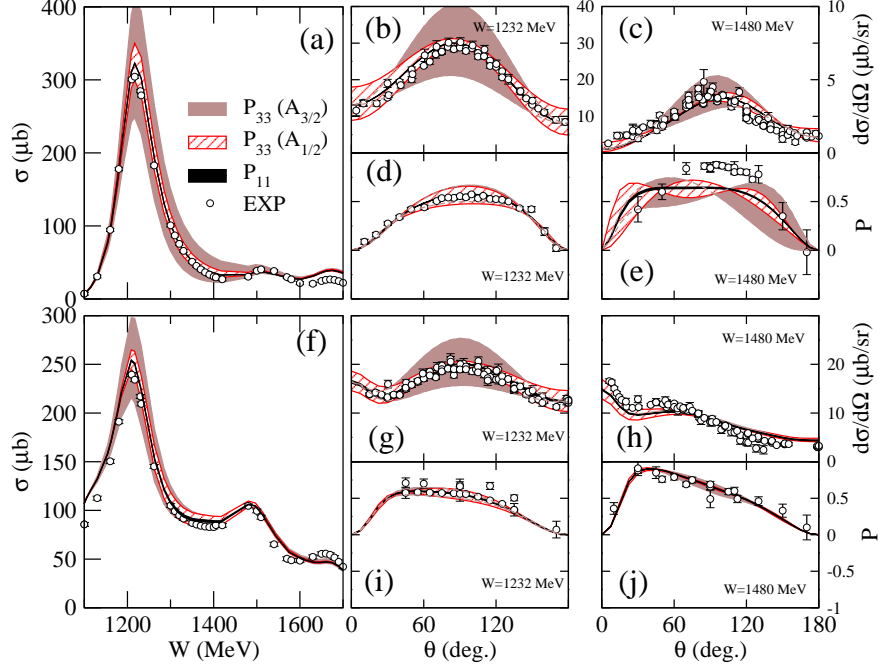


FIG. 12: The panels (a)-(e) depict the total cross section, differential cross sections and  $P$  polarization for  $\gamma p \rightarrow \pi^0 p$ , and (f)-(j) show total cross section, differential cross sections and  $P$  polarization for  $\gamma p \rightarrow \pi^+ n$ . Each band is obtained by allowing a 50% variation of the helicity amplitudes for the  $A_{3/2}$  of  $P_{33}(1232)$  (solid brown),  $A_{1/2}$  of  $P_{33}(1232)$  (oblique-lined red), and  $A_{1/2}$  of  $P_{11}(1440)$  (solid black) listed in Table I. The data are taken from Ref. [21].

the double pion photoproduction case, which is of similar size to the  $\pi N \rightarrow \pi\pi N$  case.

It is noted that our current model describes the single pion photoproduction observables in the same energy region quite well. We thus have examined the origins of our disagreements with the data by considering both the single and double photoproduction reactions. We have found that the  $\pi N\Delta$  coupling constant  $g_{\pi N\Delta}$  in the  $\gamma N \rightarrow MB$  transition matrix element plays an important role. If we reduce its strength determined in Ref.[3] by 25 % to a value close to the quark model value, the magnitude of the  $\gamma p \rightarrow \pi^+\pi^-p$  total cross section is drastically reduced, while the corresponding changes in the single pion photoproduction observables are negligible. This finding indicates that a smaller value of  $g_{\pi N\Delta}$  will be needed in a combined analysis of the world data of  $\pi N, \gamma N \rightarrow \pi N, \pi\pi N$  reactions.

We have also investigated the sensitivity of each  $\gamma N \rightarrow N^*$  process to the  $\gamma N \rightarrow \pi N$  and  $\gamma N \rightarrow \pi\pi N$  reactions. The  $\gamma N \rightarrow S_{11}(1535)$ ,  $\gamma N \rightarrow S_{31}(1620)$  and  $\gamma N \rightarrow D_{13}(1520)$  processes are found to have significant influence both on the single and double pion photoproduction observables. In particular,  $\gamma N \rightarrow D_{13}(1520)$  will be key to fixing the overestimation at the first peak of  $\gamma N \rightarrow \pi^0\pi^0 p$  around  $W = 1.5$  GeV. As for the  $P$  wave resonances, the  $\gamma N \rightarrow \Delta(1232)$  process is critical for describing the  $\gamma N \rightarrow \pi N$  observables up to  $W = 1.5$  GeV, while it plays almost no role for the total cross sections and invariant mass distributions of  $\gamma N \rightarrow \pi\pi N$  reactions. The  $\gamma N \rightarrow N^*(1440)$  process just has a negligible contribution to the  $\gamma N \rightarrow \pi N, \pi\pi N$  observables considered in this paper. The  $N^*$  states that are found to be important in determining the single and double photoproduction reactions are indicated in the second and third columns of Table I.

The results in this paper clearly show that in general the analysis of the single pion

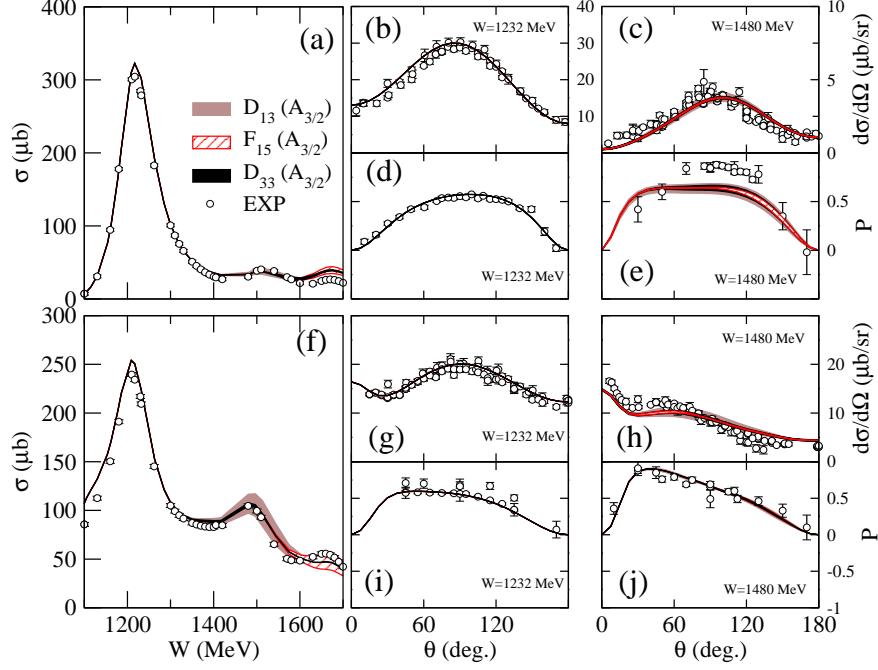


FIG. 13: The panels (a)-(e) depict the total cross section, differential cross sections and  $P$  polarization for  $\gamma p \rightarrow \pi^0 p$ , and (f)-(j) show total cross section, differential cross sections and  $P$  polarization for  $\gamma p \rightarrow \pi^+ n$ . Each band is obtained by allowing a 50% variation of the helicity amplitudes for the  $A_{3/2}$  of  $D_{13}(1520)$  (solid brown),  $A_{3/2}$  of  $F_{15}(1680)$  (oblique-lined red), and  $A_{3/2}$  of  $D_{33}(1700)$  (solid black) listed in Table I. The data are taken from Ref. [21].

production reactions is not enough to pin down the amplitudes associated with the electromagnetic interactions. In order to extract the reliable information on the  $N^*$  states below  $W = 2$  GeV, at least one needs to perform simultaneous analysis of the single and double pion production reactions. Currently, this is one of the main efforts at EBAC.

### Acknowledgments

The authors would like to thank Dr. V. Moiseev for sending the invariant mass distribution data from CLAS. This work is supported by the U.S. Department of Energy, Office of Nuclear Physics Division, under contract No. DE-AC02-06CH11357, and Contract No. DE-AC05-06OR23177 under which Jefferson Science Associates operates Jefferson Lab, by the Japan Society for the Promotion of Science, Grant-in-Aid for Scientific Research(C) 20540270, and by a CPAN Consolider INGENIO CSD 2007-0042 contract and Grants No. FIS2008-1661 (Spain). This work used resources of the National Energy Research Scientific Computing Center which is supported by the Office of Science of the U.S. Department of Energy under Contract No. DE-AC02-05CH11231.

- 
- [1] V. Burkert and T.-S. H. Lee, Int. J. of Mod. Phys. **E13**, 1035 (2004).  
[2] A. Matsuyama, T. Sato, and T.-S. H. Lee, Phys. Rep. **439**, 193 (2007).

- [3] B. Juliá-Díaz, T.-S. H. Lee, A. Matsuyama, and T. Sato, *Phys. Rev. C* **76**, 065201 (2007).
- [4] B. Juliá-Díaz, T.-S. H. Lee, A. Matsuyama, T. Sato, and L. C. Smith, *Phys. Rev. C* **77**, 045205 (2008).
- [5] B. Juliá-Díaz, H. Kamano, T.-S. H. Lee, A. Matsuyama, T. Sato, N. Suzuki, *Phys. Rev. C* **80**, 025207 (2009).
- [6] H. Kamano, B. Juliá-Díaz, T.-S. H. Lee, A. Matsuyama, and T. Sato, *Phys. Rev. C* **79**, 025206 (2009).
- [7] ABBHHM Collaboration, *Phys. Rev.* **175**, 1669 (1968).
- [8] A. Braghieri *et al.*, *Phys. Lett. B* **363**, 46 (1995).
- [9] M. Wolf, *et al.*, *Eur. Phys. J. A* **9**, 5, (2000).
- [10] W. Langgärtner, *et al.*, *Phys. Rev. Lett.* **87**, 052001, (2001).
- [11] Y. Assafiri *et al.*, *Phys. Rev. Lett.* **90**, 222001 (2003).
- [12] J. Ahrens *et al.* (GDH and A2 Collaborations), *Phys. Lett. B* **551**, 49 (2003).
- [13] J. Ahrens *et al.* (GDH and A2 Collaborations), *Phys. Lett. B* **624**, 173 (2005).
- [14] M. Bellis *et al.* (CLAS Collaboration), in *Proceedings of NSTAR2004 Workshop, Grenoble, 2004*, edited by J.-P. Bocquet, V. Kuznetsov, and D. Rebreyend (World Scientific) p. 189.
- [15] J. A. Gomez Tejedor and E. Oset, *Nucl. Phys. A* **600**, 413 (1996); *Nucl. Phys. A* **571**, 667 (1994).
- [16] K. Ochi, M. Hirata and T. Takaki, *Phys. Rev. C* **56**, 1472 (1997).
- [17] J. C. Nacher, E. Oset, M. J. Vicente Vacas and L. Roca, *Nucl. Phys. A* **695**, 295 (2001).
- [18] A. Fix and H. Arenhovel, *Eur. Phys. J. A* **25**, 115 (2005).
- [19] M. Benmerrouche and E. Tomusiak, *Phys. Rev. Lett.* **73**, 400 (1994).
- [20] V. Bernard, N. Kaiser, U. G. Meissner and A. Schmidt, *Nucl. Phys. A* **580**, 475 (1994).
- [21] CNS Data Analysis Center, George Washington University, <http://gwdac.phys.gwu.edu>.